Volume 6 | Number 26 | 14 July 2018 | Pages 4267–4388

# Journal of Materials Chemistry B

Materials for biology and medicine

rsc.li/materials-b

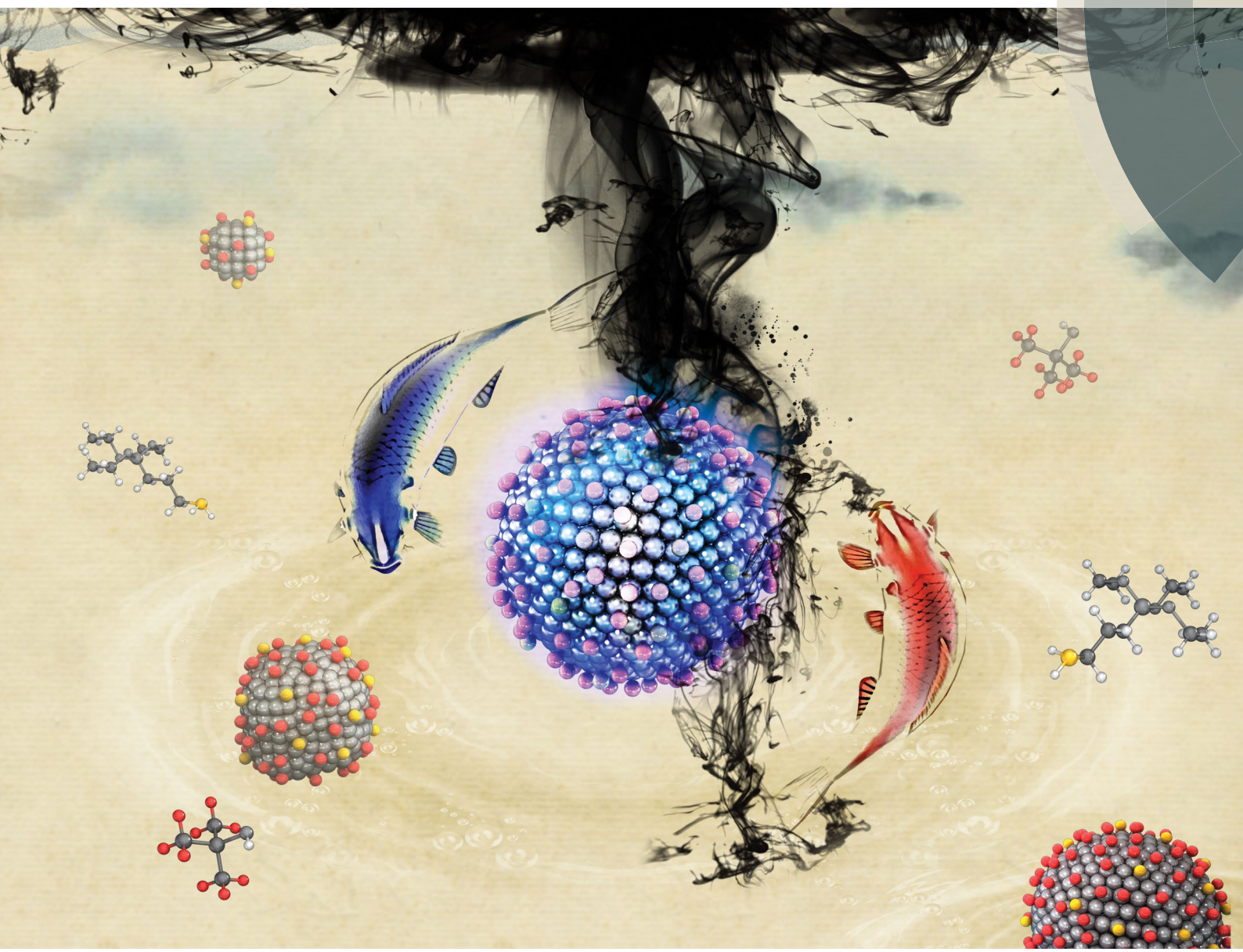

ISSN 2050-750X

ROYAL SOCIETY OF CHEMISTRY

PAPER

Shizhen Chen, Xin Zhou *et al.*

Potential detection of cancer with fluorinated silicon nanoparticles in $^{19}F$ MR and fluorescence imaging

Journal of Materials Chemistry B

PAPER

View Article Online
View Journal | View Issue



Cite this: J. Mater. Chem. B, 2018, 6, 4293

# Potential detection of cancer with fluorinated silicon nanoparticles in $^{19}$F MR and fluorescence imaging†

Sha Li,[a] Yaping Yuan,[a] Yuqi Yang,[a] Conggang Li,[a] Michael T. McMahon,[bc] Maili Liu,[a] Shizhen Chen*[a] and Xin Zhou*[a]

Received 9th March 2018,
Accepted 29th May 2018

DOI: 10.1039/c8tb00648b

rsc.li/materials-b

Fluorescence is widely used for cell imaging due to its high sensitivity and rich color choices but limited for *in vivo* imaging because of its low light penetration. Meanwhile, magnetic resonance imaging (MRI) is widely applied for *in vivo* diagnosis but not suitable for cell imaging because of its low resolution. As a result of rare background in living organisms, $^{19}$F-MRI stands out in several fields of clinical application. Herein, we report a one-pot microwave synthesis of fluorinated silicon nanoparticles ($^{19}$FSiNPs), for detection of cancer cells and tumors. Based on the quantum effects of the nano-sized nanoparticles, $^{19}$FSiNPs can act as a label free dye for ultracontrast cell fluorescence imaging. Our experiments demonstrated that these nanoprobes significantly enhanced *in vivo* $^{19}$F/$^{1}$H MRI contrast in rats with non-small cell lung tumors. Moreover, the resulting $^{19}$FSiNPs exhibited high water dispersibility and excellent biocompatibility, which make them promising for both cell imaging and *in vivo* imaging applications.



## Introduction

In recent years, the combination of optical imaging and magnetic resonance imaging (MRI) has invoked great interest in biological and medical applications. As a noninvasive molecular imaging modality, MRI produces exceptional spatial and anatomical resolution images and enables unbiased assessment of tissue physiology and pathology without depth limitations. However, it suffers the drawback of low sensitivity and poor specificity.[1–3] On the contrary, optical imaging provides real-time images with high sensitivity and specificity but with poor quantification as well as limited tissue penetration depth. Thus, integration of these two complementary imaging modalities into a novel MRI/fluorescence dual-imaging agent will significantly benefit the monitoring of molecular and cellular events in living organisms.

Generally, $^{1}$H-MRI uses exogenous contrast agents which contain Gd(III),[4–6] Mn(II)[7–9] chelates or superparamagnetic iron oxide (SPIO) nanoparticles[10–12] to modulate the relaxation of surrounding protons, providing enhanced image contrast with high potential for cancer imaging. Although such contrast agents have significantly improved MRI performance, the intense proton background sometimes causes insufficient discrimination of tumor tissues from healthy tissues. One of the most studied strategies to overcome these issues is the development of a "second color" or "hot spot" imaging using heteronuclear MRI atoms, such as $^{13}$C, $^{23}$Na, $^{31}$P, or $^{19}$F in addition to $^{1}$H. In this case, the magnetic resonance effect of the additional element adds a second colored layer with independent information about the anatomical details provided by the corresponding gray-scale $^{1}$H image. With its extremely favorable NMR properties, $^{19}$F seems to be a very promising imaging nucleus.[13–17] Fluorine offers an intense MR sensitivity (83% relative to $^{1}$H) due to its high natural abundance and high gyromagnetic ratio (40.03 MHz T$^{-1}$, 94% relative to $^{1}$H). Moreover, there is nearly no detectable endogenous fluorine, which leads to a low background signal in the living body, resulting in extremely high specificity and sensitivity.[18] For all of these reasons, a variety of $^{19}$F contrast agents (CAs) have been recently investigated for early diagnosis of cancer.[16,19–21]

Some fluorine organic molecules, such as perfluorocarbons (PFCs), were reported to be used as $^{19}$F CAs, because of their strong MRI signal as well as their chemical and biological inertness.[22–25] However, the amphiphobic characteristics of fluorous compounds make it difficult to stabilize them in a form suitable for cell uptake.[26] Typically, researchers emulsify PFCs into lipid micro/nano-particle formulations by introducing surfactants or

[a] Key Laboratory of Magnetic Resonance in Biological Systems, State Key Laboratory of Magnetic Resonance and Atomic and Molecular Physics, National Center for Magnetic Resonance in Wuhan, Wuhan Institute of Physics and Mathematics, Chinese Academy of Sciences, Wuhan 430071, China. E-mail: chenshizhen@wipm.ac.cn, xinzhou@wipm.ac.cn
[b] Russell H. Morgan Department of Radiology and Radiological Science, The Johns Hopkins University School of Medicine, Baltimore, Maryland 21287, USA
[c] F.M. Kirby Research Center for Functional Brain Imaging, Kennedy Krieger Institute, Baltimore, Maryland 21287, USA

† Electronic supplementary information (ESI) available. See DOI: 10.1039/c8tb00648b

high-energy techniques such as microfluidization to make them disperse in water, but the accompanying droplet heterogeneity and the instability of the emulsions originating from molecular diffusion induced particle size expansion have further impaired the performance of these nanoemulsions.[27] Moreover, the magnetic resonance signal from PFC emulsions almost always splits into multiple peaks which may decrease the effective fluorine concentration and reduce signal intensity.[25] In view of the potential importance of $^{19}$F-MRI, new $^{19}$F probe design strategies are needed for early monitoring of cancer diseases to overcome the shortcomings of perfluorocarbon formulations.

The main challenge, however, is to fabricate a facile $^{19}$F CAs design strategy for rendering these with excellent water solubility and a high payload of fluorine atoms, and enabling a variety of surface functionalization. The introduction of nanomaterials circumvents the drawbacks of small molecule based $^{19}$F CAs, and provides another concept for high sensitivity $^{19}$F-MRI.[21,28–30] Pasquato *et al.* first fabricated fluorinated amphiphilic thiolate coated gold nanoparticles with favorable water solubility.[28] Although a large amount of fluorine was freighted, the peaks split, resulting in broad and weak signals which produced additional imaging artifacts. Construction of multifunctional imaging probes by attaching perfluorocarbon (PFC) onto quantum dots has also been reported[31] and given access to both multispectral MR and multicolor optical imaging modalities, but the safety concerns induced by heavy metal ions in II/VI QDs are still not satsifactory. Alternatively, we focused on silicon functional nanomaterials which have shown great promise in myriads of applications due to their intrinsic advantages, such as high abundance, low cost, minimal toxicity and favorable biocompatibility.[32,33] The zero-dimensional fluorescent silicon nanoparticles (SiNPs) have been intensively studied for biomedical applications as biological labeling agents because of their unique optical properties. Compared to traditional organic fluorochromes, fluorescent SiNPs show strong fluorescence and ultrahigh photostability which was validated to be suitable for long-term and real-time imaging of cells.[34,35] The nano sized SiNPs offer greater bioimaging applications because of easy tissue penetration and effective avoidance of reticuloendothelial system uptake *in vivo*. In addition, the nano size results in rapid and efficient urinary excretion and thus lower potential toxicity.[36] Besides, in parallel with a growing interest in their design and synthesis, water soluble fluorescent SiNPs can now be conveniently synthesized and variably functionalized for a wide range of applications. Inspired by these advantages, we propose that fluorescent SiNPs could be utilized as an ideal candidate for fluorine based scaffolds.

Herein, we present a one-pot microwave synthesis to fabricate fluorinated silicon nanoparticles ($^{19}$FSiNPs) that can serve as dual $^{19}$F-MRI and fluorescence bimodal imaging agents for labeling of cancer cells. The chemically and magnetically equivalent $^{19}$F molecules grafted on the SiNPs provide $^{19}$F-based MR imaging capability, while the fluorescent SiNPs enable ultracontrast *in vitro* cellular imaging without requiring additional doping with fluorescent species. As expected, the $^{19}$FSiNPs exhibited strong fluorescence, high $^{19}$F-MRI sensitivity, favorable bio compatibility and excellent aqueous solubility. *In vivo* tests showed that the $^{19}$FSiNPs were suitable for $^{19}$F-MRI and fluorescence imaging of tumors.

# Experimental

## Materials

(3-Aminopropyl)trimethoxysilane (97%), trisodium citrate dihydrate (≥99.0%), perfluoro-*tert*-butyl alcohol (98%), and sulfosuccinimidyl 4-(*N*-maleimidomethyl)cyclohexane-1-carboxylate (Sulfo-SMCC) were purchased from J&K Scientic Ltd. Peptide cyclo-(Arg-Gly-Asp-D-Tyr-Cys) (c-(RGDyC)) was purchased from GL Biochem (Shanghai, China). Dialysis bags ($M_r$ 1000 Da and 3500 Da) were purchased from Biosharp (Hefei, China). Human lung adenocarcinoma cell line A549 and breast cancer cell line MCF7 were obtained from the Cell Bank of Chinese Academy of Sciences (Shanghai, China). Nucleic acid stain RedDot2 was purchased from Biotium.

## Apparatus

The Monowave 300 microwave system used for synthesizing the fluorinated silicon nanoparticles ($^{19}$FSiNPs) was made by Anton Paar, Austria. Exclusive vitreous vessels with a volume of 30 mL were equipped to the system to provide security during reactions demanding high temperature and pressure. Transmission electron microscopy (TEM) images were acquired *via* a JEM-2100 (HR) TEM with a LaB6 filament at an accelerating voltage of 200 kV. TEM and HRTEM samples were prepared by dispersing the sample onto carbon-coated copper grids upon evaporating the excess solvent. Energy-dispersive X-ray (EDX) spectroscopy was utilized to determine the fraction of the resultant materials. Light-scattering analysis was performed by using a DynaPro dynamic light scatter (DLS), which was made by Malvern Corp, UK (ZEN3690). The chemical composition of the $^{19}$FSiNPs was determined by an ESCALAB 220i-XL X-ray photoelectron spectrometer (XPS) (VG Scientific Ltd). For FTIR measurements, a mixture of KBr and $^{19}$FSiNPs solid samples was ground into a powder and pressed into a slice. UV-vis absorption spectra were recorded on an Evolution 220 spectrophotometer (Thermo fisher scientific). Fluorescence spectra were recorded on an Edinburgh FS5 fluorescence spectrophotometer. Optical measurements were performed at room temperature under ambient air conditions. The concentration of cells was confirmed by an auto cellometer K2 from Nexcelom (Lawrence, MA, USA). All the fluorescence imaging experiments at the cell level were finished on a laser scanning confocal microscope Nikon A1 (Nikon, Tokyo, Japan). *In vivo* fluorescence imaging was performed on an SI Imaging system (Spectral Amix). All *in vitro* and *in vivo* $^{19}$F-MRI experiments were performed on a 9.4 T Micro-imaging system (Bruker Avance 400, Ettlingen, Germany).

## Synthesis of fluorinated silicon nanoparticles ($^{19}$FSiNPs)

A one-pot microwave approach was employed to fabricate fluorinated silicon nanoparticles.[35] Firstly, the $^{19}$FSiNPs precursor was prepared by adding 4.11 mL of (3-aminopropyl)trimethoxysilan (APS) to 15 mL of high purity water dissolved with 0.697 g trisodium citrate dihydrate. The mixture was sonicated for 5 min. Then, unhydrated alcohol dissolved with perfluoro-*tert*-butyl alcohol was added to the mixture quickly followed by sonication for

 

5 min to get a homogeneous solution. The mixed solution was transferred to an exclusive vitreous vessel with a volume of 30 mL. Finally, blue emitting $^{19}$FSiNPs were prepared under 200 °C for 60 min. After cooling to room temperature, the obtained mixture was further dialyzed (1000 Da) in high purity water to fully remove impurities with molecular weight smaller than 1000 Da, such as unreacted APS molecules, trisodium citrate dihydrate molecules and perfluoro-*tert*-butyl alcohol molecules.

The as-prepared $^{19}$FSiNPs displayed intense blue color fluorescence under 365 nm UV irradiation. To determine the concentration of $^{19}$FSiNPs, the obtained mixture was filtered through a 0.22 μm microporous filter, followed by treatment of freeze-drying to obtain the $^{19}$FSiNPs solid powder. Afterwards, the required concentration of $^{19}$FSiNPs aqueous solution with blue luminescence was investigated for cellular fluorescence imaging, cellular $^{19}$F-MRI and *in vivo* $^{19}$F-MRI assessments.

$^{19}$FSiNPs covered with plentiful amino groups were gradually tagged with sulfhydryl containing c(RGDyC) by using sulfo-SMCC as a cross-linker.[35] In brief, sulfo-SMCC (10 mM in pH = 7.4 PBS) was first added to 100 μL of a dispersion of $^{19}$FSiNPs (30 mg mL$^{-1}$ in pH 7.4 PBS). The mixed solution was then incubated at 25 °C for 1 h under gentle stirring. The resultant mixture was transferred to a 3 kDa ultrafiltration tube for purifying at 6500 rpm for 15 min twice with phosphate buffer (pH = 6.8) to remove residual sulfo-SMCC. Afterwards, $\alpha_v\beta_3$ integrin targeting peptide c(RGDyC) (preresolved in pH = 6.8 PBS, 10 mM) was subsequently added to the sulfo-SMCC modified $^{19}$FSiNPs and reacted at room temperature in the dark for another 4 h, producing the RGD tagged $^{19}$FSiNPs ($^{19}$FSiNPs-RGD). The resultant mixture was further purified by centrifugation at 6500 rpm, for 15 min several times in 3 kDa Nanosep centrifugal devices, until the absorbance at 275 nm tested in the below solution passing through the ultrafiltration membrane was nearly zero. The purified $^{19}$FSiNPs in the upper solution was redispersed in PBS, and stored at 4 °C in the dark for the following studies.

### Cellular imaging

A549 cells and MCF-7 cells were cultured in RPMI 1640 medium (Boster, China), supplemented with 10% fetal bovine serum (Boster, China) and antibiotics (100 μg mL$^{-1}$ penicillin and 100 μg mL$^{-1}$ streptomycin, Boster, China) in humidified air with 5% $CO_2$ at 37 °C.

A549 (integrin $\alpha_v\beta_3$-Positive) cells at a density of $2 \times 10^5$ mL$^{-1}$ were seeded in a 6-well chamber slide with one piece of cover glass at the bottom of each chamber and then incubated overnight, followed by co-incubation with the fresh medium containing $^{19}$FSiNPs and $^{19}$FSiNPs-RGD (2 mg mL$^{-1}$) for different times. Then, the cells were washed with PBS three times to remove extra solution. To achieve fixation, A549 cells were immersed in 4% paraformaldehyde for 10 min. For staining of nuclei, the fixed A549 cells were incubated with 1× RedDot2 for 30 min. Finally the stained cells were mounted on slides in fluoromount with coverslips. The fluorescence images were acquired by confocal laser scanning microscope (A1R/A1, Nikon, Japan). For MCF-7 cell imaging, the manipulations were identical to those mentioned above.

### Cell viability

The cytotoxicity of $^{19}$FSiNPs and $^{19}$FSiNPs-RGD was evaluated *via* the methylthiazolytetrazolium (MTT) assay against the cultured A549 and MCF-7 cell lines. Briefly, A549 cells were seeded into 96-well plates at a density of $5 \times 10^4$ cells per well and incubated overnight for cell attachment. $^{19}$FSiNPs and $^{19}$FSiNPs-RGD were diluted with the medium to specific concentrations (UV absorption at 335 nm was 0.8, 0.4, 0.2, 0.1, and 0.05 respectively) and added to the well, which was followed by co-incubation at 37 °C for 4 h under 5% $CO_2$. The cells were then washed twice with PBS and further incubated in fresh culture medium for an additional 44 h. Thereafter, 3-((4,5-dimethylthiazol-2-yl)-2,5-diphenyltetrazolium bromide) (MTT) was added to the culture medium with the final concentration of 0.5 mg mL$^{-1}$ and incubated at 37 °C for another 4 h. 200 μL DMSO was added per well after removing the medium and shaken for 30 min to fully dissolve the colored formazan, which was produced by cellular reduction of MTT (reduction takes place only in living cells when the mitochondrial reductases are active). The absorbance of the solution in each well was measured at 490 nm by using an ELISA plate reader (Spectra MAX 190, Molecular Devices, USA).

### $^{19}$F-NMR measurements

Nanoparticles were prepared in 90% distilled water and 10% $D_2O$. All of the $^{19}$F NMR experiments were performed on a Bruker AMX-500 NMR spectrometer. $CF_3SO_3Na$ was used as an internal standard to determine the content of fluorine atoms in the nanoparticles. Briefly, the mixture of $^{19}$FSiNPs and $CF_3SO_3Na$ was placed in an NMR tube, and one-dimensional (1D) $^{19}$F spectra were acquired on a 500 MHz spectrometer. The $^{19}$F spectra displayed two narrow major peaks, one each for $^{19}$FSiNPs and $CF_3SO_3Na$. The ratio of the integrated areas under these two peaks was used to calculate the mean $^{19}$F content.

The inversion-recovery experiments were employed to measure the longitudinal time $T_1$, and CPMG (Carr–Purcell–Meiboom–Gill) experiments were performed to measure the transverse relaxation time $T_2$.

### Cell experiment for $^{19}$F-MRI

A549 cells were cultured in RPMI 1640 medium (Boster, China) containing 10% fetal bovine serum at 37 °C under 5% $CO_2$. The regular culture medium was removed when the cell confluence reached 90–100%. Serum-free culture medium containing the $^{19}$FSiNPs and $^{19}$FSiNPs-RGD ($C_F$ = 15 mM) was added. After co-incubation for a further 1 h at 37 °C, $9 \times 10^7$ cells were harvested with trypsin–EDTA and mixed with PBS. Afterwards, the cells were centrifuged (1000 rpm, 5 min) and washed with PBS to remove the remaining probe. Then the cells were lysed by using 1 mL of radio immunoprecipitation assay (RIPA) lysis buffer for 2 h, and the supernatants were collected for $^{19}$F-MRI assessment.

### *In vivo* $^{19}$F-MRI and fluorescence imaging

BALB/c male nude mice (aged 5–6 weeks, 18–21 g body weight) were purchased from Human SJA Laboratory Animal Co., Ltd. All experimental protocols in this study were approved by the

Animal Care and Use Committees at the Wuhan Institute of Physics and Mathematics, the Chinese Academy of Sciences. To prepare tumor-bearing mice, A549 cells were centrifuged and resuspended in PBS to a concentration of $1 \times 10^7$ cells per mL. Then the mice were inoculated subcutaneously with 100 μL A549 cell suspension solution on the left hind leg and allowed to grow for 2 weeks; typically, a solid tumor is formed during this period. For *in vivo* $^{19}$F-MRI imaging, living mice were firstly anesthetized by intraperitoneal injection of 150 μL 1% pelltobarbitalum natricum (in PBS). The mice bearing tumors were then administered with 100 μL of $^{19}$FSiNPs solution ($C_F$ = 650 mM) through intratumor injection and the MRI measurements were carried out on 400 M Bruker BioSpec MRI system. The RARE (rapid acquisition with refocused echoes) method was employed for $^1$H MRI. The parameters for $^1$H MRI were set as follows: number of average = 4, TR (repetition time) = 1500 ms, TE (effective time) = 8.2 ms, FOV (field of view) = 40 mm × 40 mm, SI (slice thickness) = 2 mm, matrix size = 256 × 256. Correspondingly, the RARE method was applied for $^{19}$F-MRI, and the parameters were as follows: number of average = 64, TR/TE = 3500 ms/8.15 ms, FOV = 40 mm × 40 mm, SI = 20 mm, matrix size = 64 × 64, and the total scan time was approximately 30 min. For *in vivo* fluorescence imaging, tumor bearing mice (left foreleg) were administered 200 μL of $^{19}$FSiNPs solution (10 mg mL$^{-1}$ in PBS) through intratumor injection and the fluorescence imaging measurements were carried out on an SI Imaging system (Spectral Amix). The excitation wavelength was 360 nm, and the emission filter wavelength was 490 nm.

## Results and discussion

### Morphology and surface characterization of $^{19}$FSiNPs

$^{19}$FSiNPs were produced by a simple one-pot microwave-assisted reaction as illustrated in Scheme 1. In a typical reaction, (3-aminopropyl)trimethoxysilane (APS) was gradually reduced by trisodium citrate (methoxy groups of APS were reduced to hydroxy groups) and further linked with perfluoro-*tert*-butyl alcohol under microwave irradiation. As the reaction proceeded, crystal nuclei were formed slowly and uniformly which was favorable for surface ordering and improving monodispersity. The Ostwald ripening stage[35,36] occurred along with the formation of many small particles. Afterwards, the smaller crystals act as fuel for the growth of bigger crystals with smaller surface-to-volume ratios, reducing the energy of the entire system, and finally producing stable fluorinated silicon nanoparticles with larger size. The prepared $^{19}$FSiNPs exhibited excellent water solubility without additional surface modification.

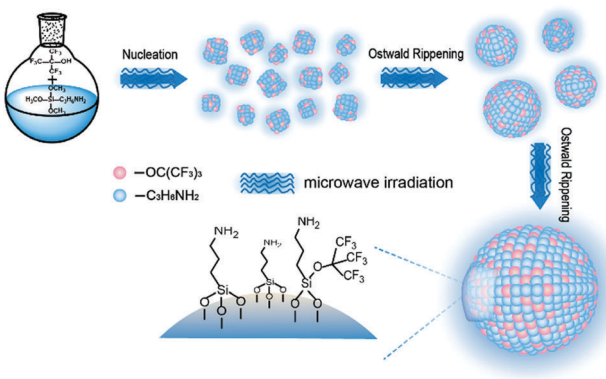


Scheme 1 Schematic illustration depicting one-pot microwave synthesis of fluorinated silicon nanoparticles ($^{19}$FSiNPs).

Typical transmission electron microscopy (TEM) images of $^{19}$FSiNPs are shown in Fig. 1(a), in which the resultant $^{19}$FSiNPs were nearly spherical in shape without obvious aggregation. The particles in the inset of Fig. 1(b) clearly show the crystalline nature of the SiNPs, with lattice fringes for the [220] *d*-spacing, 1.91 Å. The selected area electron diffraction (SAED) pattern for $^{19}$FSiNPs (Fig. S1, ESI†) can be indexed to the [111], [220] and [311] diffraction rings and is in good agreement with the face-centered cubic structure.

The average particle diameter was found to be 3.85 ± 1.57 nm by measuring more than 200 particles as indicated in Fig. 1(c). Dynamic light scattering (DLS) measurements indicated that the average hydrodynamic diameter of the $^{19}$FSiNPs was 5.37 ± 3.2 nm with a low PDI value of 0.212 as shown in Fig. 1(d). Particularly, $^{19}$FSiNPs possess such ultrasmall-size (<5 nm) because of the surface covered hydrophilic ligands with short chains (most –$NH_2$), which are favorable for *in vivo* bioapplications (NPs with hydrodynamic diameters smaller than 10.0 nm are found to be more rapidly and efficiently eliminated from mice through renal clearance).[37]

To characterize the surface groups of the modified $^{19}$FSiNPs, FTIR spectra of the $^{19}$FSiNPs, perfluoro-*tert*-butyl alcohol, trisodium citrate dihydrate and APS were further measured in our experiment, which featured several distinct absorption peaks in the range of 600–4000 cm$^{-1}$ (Fig. 1(e) and Fig. S2, ESI†). Typically, for perfluoro-*tert*-butyl alcohol (green line), the characteristic FTIR peaks for the –$C(CF_3)_3$ group are located at 1100–1350 cm$^{-1}$. For APS (blue line), the strong FTIR absorbance peaks at 1080, 1390–1440, 1580, 3000, and 3400 cm$^{-1}$ are assigned to the vibrational stretches of Si–O bonding, C–O vibration, N–H bending vibrations, C–H vibration, and N–H stretching vibration, respectively. For the $^{19}$FSiNPs (red line), the sharp absorbance peak at 1080 cm$^{-1}$ is ascribed to the vibrational stretch of Si–O bonding, and the strong absorbances at 1580, 3000, and 3400 cm$^{-1}$ are assigned to N–H bending vibrations, C–H vibration, and the N–H stretching vibration, respectively. In particular, the weak absorbance peak at 1232 cm$^{-1}$ is ascribed to C–F vibration. The FTIR results demonstrated the existence of C–F bonds in $^{19}$FSiNPs. The EDX pattern confirms the presence of C, Si, N, O, and F elements in the $^{19}$FSiNPs (Fig. S3, ESI†). $^1$H and $^{13}$C NMR of the $^{19}$FSNPs was further carried out to characterize the nanoparticles (Fig. S4 and S5, ESI†). X-ray photoelectron spectra (XPS) were also measured to analyze the chemical compositions of the $^{19}$FSiNPs compared to SiNPs (Fig. 1(f)). The results showed intense emissions at 102.26, 284.8, 399.07, and 531.87 eV, suggesting the presence of Si, C, N and O atoms respectively both in the $^{19}$FSiNPs and SiNPs. The emission at around 102 eV is routinely attributed to functionalized Si sub-oxides (Fig. S6, ESI†). In particular, there exists an extra emission at 688.13 eV in the XPS of the $^{19}$FSiNPs,

 

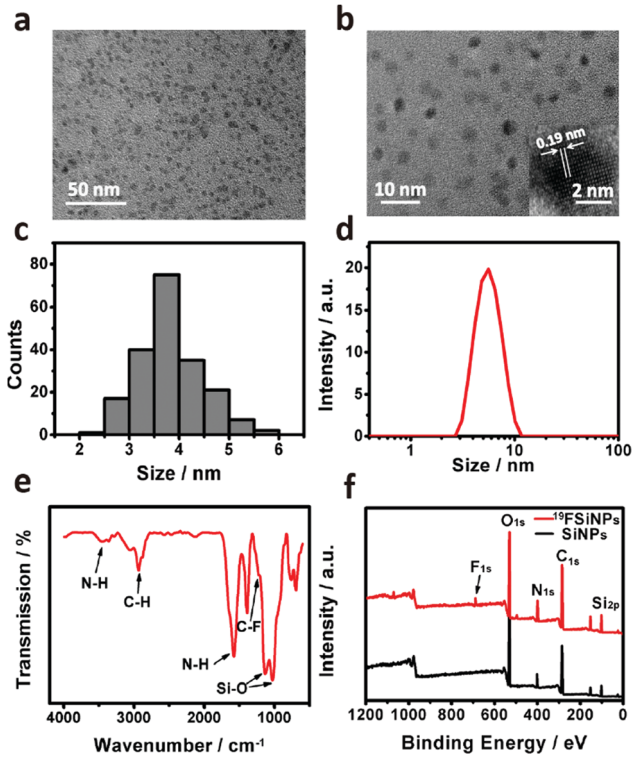


Fig. 1 Morphology and surface characterization of the $^{19}$FSiNPs. (a) TEM and (b) HRTEM images of the resultant $^{19}$FSiNPs. (c) TEM and (d) DLS diameter distribution of the $^{19}$FSiNPs. (e) FTIR spectral imaging of the $^{19}$FSiNPs. (f) XPS spectral imaging of the $^{19}$FSiNPs and SiNPs.

which is ascribed to F atoms, indicating the successful fabrication of fluorinated silicon nanoparticles. XPS analysis of the $^{19}$FSiNPs revealed that the atomic percentages of C, O, Si, N and F were 54.23, 23.52, 11.25, 9.51 and 1.48% respectively.

### Optical and magnetic characterization of the $^{19}$FSiNPs

The absorption and photoluminescence emission spectra of the synthesized $^{19}$FSiNPs were measured (Fig. 2(a)), with predominant absorption in the UV region and the strongest emission in the blue region of visible light. The $^{19}$FSiNPs exhibited excellent water solubility and featured strong blue fluorescence under UV irradiation (quantum yield value is 16.1% against that of quinine sulfate as shown in Fig. S7, ESI†), which contributed to quantum confinement and radiative recombination of such small-sized nanoparticles.[35] Of particular interest, undesired photobleaching of the $^{19}$FSiNPs did not occur over a wide range of pH values (4–10) in water and RPMI-1640 medium (Fig. S8, ESI†). The demonstrated high fluorescence intensity of the $^{19}$FSiNPs would be strongly favorable for bioimaging applications, where the loss of fluorescence because of photobleaching under acidic environments often hampers signal detection for *in vitro* cellular imaging. Additionally, the $^{19}$FSiNPs showed excellent storage stability at 4 °C over 40 days. The $^{19}$FSiNPs exhibited about 13% loss of PL intensity after 45 days of storage (Fig. S9(a), ESI†). DLS confirmed that the $^{19}$FSiNPs displayed slight aggregation after 45 days of storage as the hydrodynamic diameter increased slightly from 5.37 nm to 6.38 nm (Fig. S9(b), ESI†).

Afterwards, an $^{19}$F-NMR study on an aqueous solution of $^{19}$FSiNPs was carried out to verify their magnetic activity. As expected, the spectra exhibited a strong single peak at −75.34 ppm from the chemically and magnetically equivalent trifluoromethyl groups grafted on the surface of the $^{19}$FSiNPs (Fig. 2(b)), which is important to maximize the generated magnetic resonance signal. Because of the clear $^{19}$F-NMR signal, we then determined the longitudinal relaxation time $T_1$ and the transverse relaxation time $T_2$ of the $^{19}$FSiNPs. As we all know, $T_1$ and $T_2$ are both important contrast factors for MRI, because $T_1$ determines scanning time directly and the apparent intensity of the MRI signal depends on the $T_2$ values. The $^{19}$F compound must have favorable relaxation parameters. In general, this means a short $T_1$ and preferably a long $T_2$. The $^{19}$FSiNPs showed a $T_1$ of 1.5 s and a $T_2$ of 1.0 s tested on a 500 MHz Bruker spectrometer, which were found to be in the area of seconds and still promising enough for MRI data collection. Nuclear magnetic resonance (NMR) was used to assay the $^{19}$F content. Briefly, a mixture of $^{19}$FSiNPs and $CF_3SO_3Na$ (as an NMR reference compound) was placed in an NMR tube, and a one-dimensional (1D) $^{19}$F spectrum was acquired on a 500 MHz spectrometer. The $^{19}$F spectra displayed two narrow major peaks, one each for $^{19}$FSiNPs and $CF_3SO_3Na$. The ratio of the integrated areas under these two peaks was used to calculate the mean amount of $^{19}$F grafted on the SiNPs. The weight ratio of fluorine grafted on the $^{19}$FSiNPs was calculated to be 1.52%, well in agreement with the results of XPS. It is noteworthy that the $^{19}$FSiNPs exhibited such excellent water solubility that they could be dissolved to a concentration of hundreds of milligrams per milliliter in water. To test the $^{19}$F-MRI sensitivities of the $^{19}$FSiNPs, $^{19}$F-MRI phantom experiments were then carried out as shown in Fig. 2(c); obvious $^{19}$F-MRI signals were observed from the $^{19}$FSiNP solution at different concentrations, and the signal intensity was found to be correlated with the concentration of fluorine (Fig. 2(d)), demonstrating the potential applications of

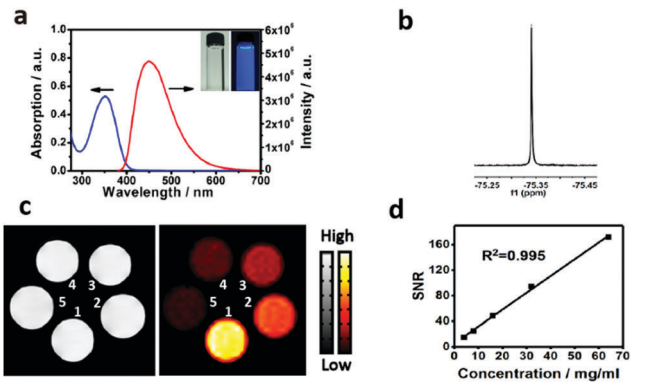


Fig. 2 Optical and magnetic resonance characterization of the $^{19}$FSiNPs. (a) UV and PL spectral imaging of $^{19}$FSiNPs; the inset of (a) is a photograph showing the $^{19}$FSiNP sample under ambient light and 365 nm UV irradiation. (b) $^{19}$F NMR spectrum of the $^{19}$FSiNP aqueous solution (10 mg mL$^{-1}$) on a 500 MHz Bruker spectrometer. (c) $^{1}$H-MRI (left) and $^{19}$F-MRI (right) of $^{19}$FSiNP aqueous solutions with various concentrations. (1-5): 64, 32, 16, 8, and 4 mg mL$^{-1}$ $^{19}$FSiNPs. (d) Plot of the $^{19}$F-MRI signal-to-noise ratio (SNR) *versus* $^{19}$FSiNP concentration.

this nanoprobe for *in vivo* MRI. These results suggest that delivery of these $^{19}$FSiNPs to tumors might be traced and visualized with a high signal-to-background ratio *via* $^{19}$F-MRI.

### Lung cancer cell targeting

The application of $^{19}$FSiNPs for *in vitro* and *in vivo* targeted tumor imaging is vitally important in the biological and biomedical fields. For targeted bioimaging, $^{19}$FSiNPs must be modified with functional species with targeting properties. The RGD peptide has been widely used as a targeting ligand to mediate specific binding to cell adhesion molecule integrin $\alpha_v\beta_3$, which is over expressed in many cancer cells (including carcinoma, sarcoma, glioblastoma and melanoma, *etc.*).[38] To further investigate the potential biomedical applications of the $^{19}$FSiNPs and $^{19}$FSiNPs-RGD, their uptake into specific cells was evaluated *via* fluorescence imaging and $^{19}$F-MRI. $\alpha_v\beta_3$-positive A549 and $\alpha_v\beta_3$-negative MCF-7 breast cancer cells were introduced to study the selectivity of the nanoconstruct. $^{19}$FSiNPs were then tagged with c(RGDyC) *via* an established reaction using sulfo-SMCC as a heterobifunctional cross-linker.[39] As illustrated in Scheme 2, the $^{19}$FSiNPs were first combined with sulfo-SMCC to yield maleimide activated $^{19}$FSiNPs. The resultant maleimide-activated $^{19}$FSiNPs were further reacted with c(RGDyC) peptides, finally producing the RGD-conjugated fluorinated silicon nanoparticles ($^{19}$FSiNPs-RGD).

After adequate removal of unreacted c(RGDyC) peptides (Fig. S10, ESI†), the hydrodynamic diameter of the $^{19}$FSiNPs-RGD was determined to be 10 nm with a PDI value of 0.24 (Fig. S11, ESI†) which was larger than that of the $^{19}$FSiNPs. The absorption spectra of the $^{19}$FSiNPs and $^{19}$FSiNPs-RGD revealed that only the $^{19}$FSiNPs-RGD had an absorption peak at 275 nm (Fig. S12(a), ESI†) which was specifically associated with the RGD moiety, indicating the successful conjugation of $^{19}$FSiNPs and c(RGDyC). In addition, $^1$H NMR of the $^{19}$FSiNPs-RGD also showed the existence of RGD on the $^{19}$FSiNPs (Fig. S13 and S14, ESI†). The weight ratio of immobilized c(RGDyC) on the $^{19}$FSiNPs was calculated to be 7% according to the calibration curve (Fig. S15, ESI†). In addition, the PL intensity of the $^{19}$FSiNPs-RGD was slightly stronger than that of the $^{19}$FSiNPs which was speculated to be derived from the different surface electronic states of the $^{19}$FSiNPs and $^{19}$FSiNPs-RGD (Fig. S12(b), ESI†).

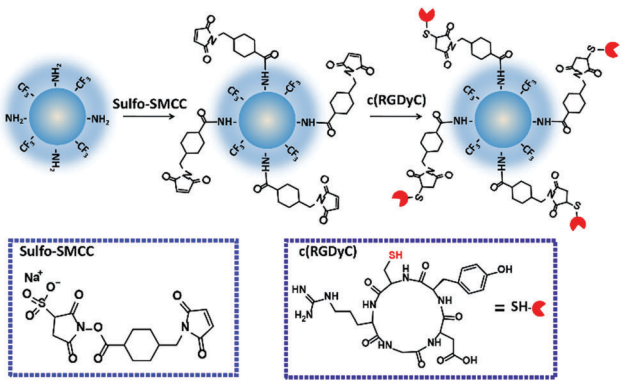


Scheme 2 Schematic synthesis of $^{19}$FSiNPs-RGD.

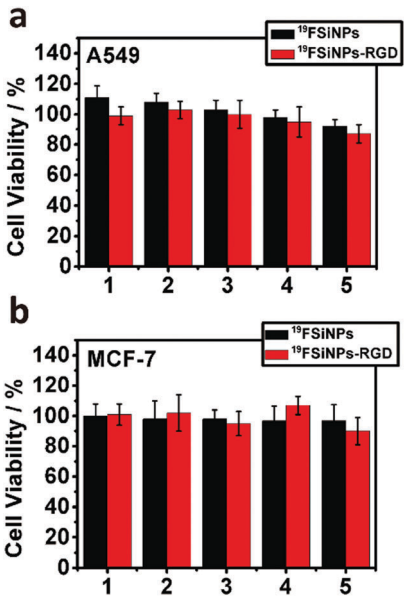


Fig. 3 *In vitro* concentration-dependent cellular viability of (a) A549 and (b) MCF-7 cells against $^{19}$FSiNPs and $^{19}$FSiNPs-RGD. The categorization of 1, 2, 3, 4 and 5 on the *X* axis represents the UV absorption at 335 nm as 0.05, 0.1, 0.2, 0.4 and 0.8 for $^{19}$FSiNPs and $^{19}$FSiNPs-RGD respectively. The viability of the control cells was considered 100%.

Although SiNPs are generally known to be biocompatible and nontoxic, the *in vitro* toxicity of the $^{19}$FSiNPs and $^{19}$FSiNPs-RGD towards A549 and MCF-7 cells was evaluated by MTT assay. As shown in Fig. 3, the viability of A549 and MCF-7 cells was not affected by up to 2 mg mL$^{-1}$ of $^{19}$FSiNPs and the same concentration of $^{19}$FSiNPs-RGD (the corresponding UV absorption values at 335 nm was 0.8), indicating that the $^{19}$FSiNPs and $^{19}$FSiNPs-RGD were non- or low-cytotoxic to A549 cells and this ensured their use as a novel theranostic agent for further cell experiments and *in vivo* applications.

To further investigate the potential biomedical applications of the $^{19}$FSiNPs and $^{19}$FSiNPs-RGD, their uptake into specific cells was evaluated *via* fluorescence imaging and $^{19}$F-MRI. The time-dependent *in vitro* behavior of the nanoparticles in A549 and MCF-7 cells was investigated *via* focal laser scanning microscopy (CLSM) as shown in Fig. S16 (ESI†), and the results indicated that nanoparticles were gradually swallowed into cells and accumulated mainly in the cytoplasm. For A549 cells with a high integrin $\alpha_v\beta_3$ expression, the fluorescence signal in the $^{19}$FSiNPs-RGD treated groups was much stronger than that of the pure $^{19}$FSiNPs treated groups (Fig. 4(a)), indicating the targeting effect of the peptide c(RGDyC). In contrast, for MCF-7 cells with a low integrin $\alpha_v\beta_3$ expression, the observed blue fluorescence of $^{19}$FSiNPs-RGD was much weaker, even for incubation times up to 4 h. These data convincingly confirmed the high affinity and integrin $\alpha_v\beta_3$-specific binding of $^{19}$FSiNPs-RGD. The nanoparticle uptake by cells was also examined *via* $^{19}$F-MRI. After incubation with $^{19}$FSiNPs and $^{19}$FSiNPs-RGD, the A549 cell lysate was collected and transferred into a 10 mm NMR tube and $^{19}$F-MRI experiments were performed. Fig. 4(b) shows that $^{19}$F-MRI signals were observed from the A549 cells

 

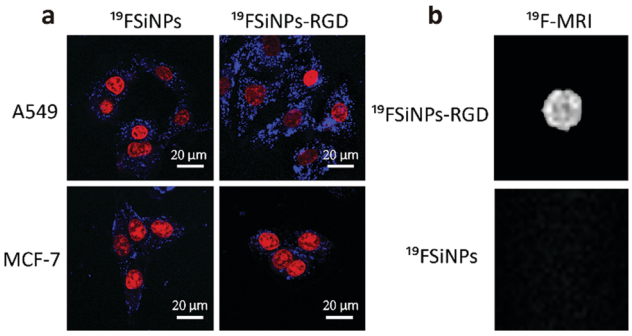


Fig. 4 (a) Fluorescence images of A549 and MCF-7 cells treated with pure $^{19}$FSiNPs and $^{19}$FSiNPs-RGD for 2 h captured *via* laser scanning confocal microscopy, where the nuclei stained with RedDot2 are shown in red. All fluorescence images were captured under the same conditions. (b) $^{19}$F-MR images of the cell lysate of A549 cells after incubation with $^{19}$FSiNPs and $^{19}$FSiNPs-RGD at 37 °C for 1 h. RIPA lysis buffer was used to ensure cell extraction.

incubated with $^{19}$FSiNPs-RGD, while no $^{19}$F-MRI signals were observed from the control group. These results demonstrated that $^{19}$FSiNPs-RGD could be used as a $^{19}$F-MRI/FI bimodal nanoprobe for targeted detection of A549 cancer cells.

### *In vivo* $^{19}$F-MRI and fluorescence imaging

For future medical or biological applications, a key step is visualization of the synthesized agents in a biological environment. So we explored the possibility of *in vivo* $^{19}$F-MRI/FI studies by injecting $^{19}$FSiNPs into the tumors of the mice. Fig. 5(a) shows the *in vivo* fluorescence imaging of the $^{19}$FSiNPs (10 mg mL$^{-1}$) in a A549 tumor bearing mouse. Bright fluorescence in the tumor area was observed, indicating the strong fluorescence intensity of the $^{19}$FSiNPs, which contribute to the quantum confinement effect. Furthermore, $^{1}$H-MRI (Fig. 5(b)) was carried out to show the anatomic structure of the mouse and the profile of the tumor. As expected, a distinct difference can be observed in the $^{19}$F-MR images after intratumor injection of $^{19}$FSiNPs ($C_F$ = 650 mM). Fluorine inside the tumor yields positive-signal "hot-spot" images, with no background signal due to the low biological abundance of fluorine in tissues. These results highlight the intrinsic sensitivity and utility of $^{19}$FSiNPs for *in vivo* $^{19}$F-MRI and fluorescence imaging of the tumor. To investigate the influence of $^{19}$FSiNPs on the organs of mice, a histopathological examination was performed using the standard histological techniques *via* hematoxylin-eosin (HE) staining in the major organs (heart, liver, spleen, lungs, and kidneys). As illustrated in Fig. 5(c), compared with the control group, there were no significant differences between various organs, indicating that the $^{19}$FSiNPs had a negligible toxic effect on the mice.

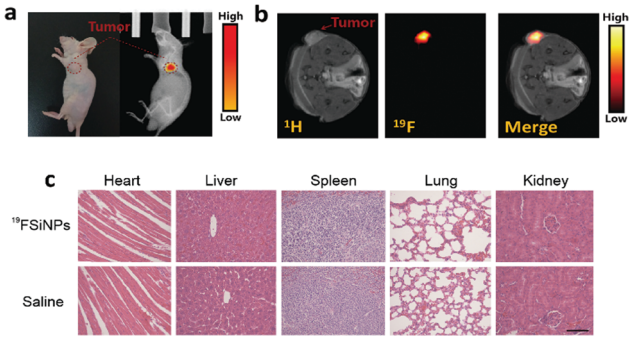


Fig. 5 *In vivo* $^{19}$F-MRI/FI studies and histopathologic examination. (a) Fluorescence image of A549 tumor-bearing mice (left foreleg) after intratumor injection of $^{19}$FSiNPs (10 mg mL$^{-1}$). (b) Anatomical $^{1}$H-MR images shown in gray (left), and $^{19}$F-MR images overlaid in false color (middle), $C_F$ = 650 mM. The tumor can clearly be depicted in the anatomical images (left hind leg) as a bright area, which co-localizes well with areas of significant $^{19}$F signal (right). (c) Histopathologic examinations of the tissues including the heart, liver, spleen, lungs, and kidneys from BALB/c nude mice after intratumor injection of $^{19}$FSiNPs ($C_F$ = 650 mM) and saline. Scale bar: 100 μm.

## Conclusions

In summary, a novel formulation of $^{19}$FSiNPs with strong fluorescence, high $^{19}$F-MRI sensitivity, favorable biocompatibility and excellent aqueous solubility has been successfully developed through a one-pot microwave synthesis strategy. The targeted dual $^{19}$F-MR/fluorescence imaging study of A549 cells was also achieved by grafting specific biological moieties such as peptides onto these nanoparticles. The high quality fluorescence of the $^{19}$FSiNPs originating from the nano-sized quantum effect also enabled the *in vivo* fluorescence imaging of tumors. In addition, the modified microwave assisted synthetic strategy abandons tedious and complicated manipulations required for synthesizing perfluorocarbon nano-emulsions. Since the prepared $^{19}$FSiNPs suffer the drawback of it's short wavelength fluorescence and relatively long longitudinal relaxation times (T1) which necessitated long scanning times, $^{19}$FSiNPs were used for *in vivo* experiments by intratumor injection. The $^{19}$FSiNPs exhibited such excellent water solubility that they can be dissolved to a concentration of hundreds of milligrams per milliliter in water, which ensures enough fluorine content for *in vivo* $^{19}$F-MRI detection of the tumor. The high quality fluorescence of $^{19}$FSiNPs originating from the nano-sized quantum effect also enabled the *in vivo* fluorescence imaging of tumor. For *in vivo* $^{19}$F-MRI, there remains room to increase the fluorine contents and optimize the relaxation time of nanoparticles. On the other hand, efforts to engineer a longer wavelength fluorescent species as fluorinated scaffold is also of quite importance and could be studied further. Consequently, the present aqueous synthesis of high-quality $^{19}$FSiNPs would facilitate a myriad of applications such as in biosensors, *in vitro* and *in vivo* imaging, *etc.*

## Conflicts of interest

The authors have declared that no competing interest exists.

## Acknowledgements

This work was financially supported by the National Natural Science Foundation of China (21575157, 81227902, 81625011), National Key R&D Program of China (2017YFA0505400, 2016YFC1304700) and

Key Research Program of Frontier Sciences, CAS, Grant No QYZDY-SSW-SLH018. X. Zhou thanks the National Program for Special Support of Eminent Professionals (National Program for Support of Top-notch Young Professionals).

## Notes and references

1 E. Terreno, D. D. Castelli, A. Viale and S. Aime, *Chem. Rev.*, 2010, **110**, 3019.
2 Z. Gao, T. Ma, E. Zhao, D. Docter, W. Yang, R. H. Stauber and M. Gao, *Small*, 2016, **12**, 556.
3 G. Angelovski, *Angew. Chem., Int. Ed.*, 2016, **55**, 7038.
4 P. Caravan, J. J. Ellison, T. J. McMurry and R. B. Lauffer, *Chem. Rev.*, 1999, **99**, 2293.
5 P. Caravan, Strategies for increasing the sensitivity of gadolinium based MRI contrast agents, *Chem. Soc. Rev.*, 2006, **35**, 512.
6 A. Moussaron, S. Vibhute, A. Bianchi, S. Gündüz, S. Kotb, L. Sancey, V. Motto-Ros, S. Rizzitelli, Y. Crémillieux, F. Lux, N. K. Logothetis, O. Tillement and G. Angelovski, *Small*, 2015, **11**, 4900.
7 M. F. Bennewitz, T. L. Lobo, M. K. Nkansah, G. Ulas, G. W. Brudvig and E. M. Shapiro, *ACS Nano*, 2011, **5**, 3438.
8 Z. Zhao, H. Fan, G. Zhou, H. Bai, H. Liang, R. Wang, X. Zhang and W. Tan, *J. Am. Chem. Soc.*, 2014, **136**, 11220.
9 A. Barandov, B. B. Bartelle, B. A. Gonzalez, W. L. White, S. J. Lippard and A. Jasanoff, *J. Am. Chem. Soc.*, 2016, **138**, 5483.
10 J. W. Bulte and D. L. Kraitchman, *Chem. Rev.*, 2004, **17**, 484.
11 H. B. Na, I. C. Song and T. Hyeon, *Adv. Mater.*, 2009, **21**, 2133.
12 B. Hu, M. Zeng, J. Chen, Z. Zhang, X. Zhang, Z. Fan and X. Zhang, *Small*, 2016, **12**, 4707.
13 E. T. Ahrens, R. Flores, H. Xu and P. A. Morel, *Nat. Biotechnol.*, 2005, **23**, 983.
14 I. Tirotta, V. Dichiarante, C. Pigliacelli, G. Cavallo, G. Terraneo, F. B. Bombelli, P. Metrangolo and G. Resnati, *Chem. Rev.*, 2015, **115**, 1106.
15 K. Yamaguchi, R. Ueki, H. Nonaka, F. Sugihara, T. Matsuda and S. Sando, *J. Am. Chem. Soc.*, 2011, **133**, 14208.
16 S. Chen, Y. Yang, H. Li, X. Zhou and M. Liu, *Chem. Commun.*, 2014, **50**, 283.
17 Y. Yuan, S. Ge, H. Sun, X. Dong, H. Zhao, L. An, J. Zhang, J. Wang, B. Hu and G. Liang, *ACS Nano*, 2015, **9**, 5117.
18 J. Ruiz-Cabello, B. P. Barnett, P. A. Bottomley and J. W. Bulte, *NMR Biomed.*, 2011, **24**, 114.
19 T. Nakamura, F. Sugihara, H. Matsushita, Y. Yoshioka, S. Mizukami and K. Kikuchi, *Chem. Sci.*, 2015, **6**, 1986.
20 H. Matsushita, S. Mizukami, F. Sugihara, Y. Nakanishi, Y. Yoshioka and K. Kikuchi, *Angew. Chem., Int. Ed.*, 2014, **53**, 1008.
21 G. Hu, N. Li, J. Tang, S. Xu and L. Wang, *ACS Appl. Mater. Interfaces*, 2016, **8**, 22830.
22 J. M. Janjic, M. Srinivas, D. K. K. Kadayakkara and E. T. Ahrens, *J. Am. Chem. Soc.*, 2008, **130**, 2832.
23 B. Ebner, P. Behm, C. Jacoby, S. Burghoff, B. A. French, J. Schrader and U. Flögel, *Circ. Cardiovasc. Imaging*, 2010, **3**, 202.
24 Y. T. Lim, M. Y. Cho, J.-H. Kang, Y.-W. Noh, J.-H. Cho, K. S. Hong, J. W. Chung and B. H. Chung, *Biomaterials*, 2010, **31**, 4964.
25 C. Jacoby, S. Temme, F. Mayenfels, N. Benoit, M. P. Krafft, R. Schubert, J. Schrader and U. Flögel, *NMR Biomed.*, 2014, **27**, 261.
26 M. Cametti, B. Crousse, P. Metrangolo, R. Milani and G. Resnati, *Chem. Soc. Rev.*, 2012, **41**, 31.
27 M. Srinivas, A. Heerschap, E. T. Ahrens, C. G. Figdor and I. J. De Vries, *Trends Biotechnol.*, 2010, **28**, 363.
28 C. Gentilini, F. Evangelista, P. Rudolf, P. Franchi, M. Lucarini and L. Pasquato, *J. Am. Chem. Soc.*, 2008, **130**, 15678.
29 M. Boccalon, P. Franchi, M. Lucarini, J. J. Delgado, F. Sousa, F. Stellacci, I. Zucca, A. Scotti, R. Spreafico, P. Pengo and L. Pasquato, *Chem. Commun.*, 2013, **49**, 8794.
30 H. Chen, M. Song, J. Tang, G. Hu, S. Xu, Z. Guo, N. Li, J. Cui, X. Zhang, X. Chen and L. Wang, *ACS Nano*, 2016, **10**, 1355.
31 Y. T. Lim, Y.-W. Noh, J.-H. Cho, J. H. Han, B. S. Choi, J. Kwon, K. S. Hong, A. Gokarna, Y.-H. Cho and B. H. Chung, *J. Am. Chem. Soc.*, 2009, **131**, 17145.
32 J.-H. Park, L. Gu, G. V. Maltzahn, E. Ruoslahti, S. N. Bhatia and M. J. Sailor, *Nat. Mater.*, 2009, **8**, 331.
33 J. G. Croissant, Y. Fatieiev and N. M. Khashab, *Adv. Mater.*, 2017, **29**, 1604634.
34 M. Montalti, A. Cantelli and G. Battistelli, *Chem. Soc. Rev.*, 2015, **44**, 4853.
35 Y. Zhong, F. Peng, F. Bao, S. Wang, X. Ji, L. Yang, Y. Su, S. T. Lee and Y. He, *J. Am. Chem. Soc.*, 2013, **135**, 8350.
36 Y. He, H. Lu, L. Sai, W. Lai, Q. Fan, L. Wang and W. Huang, *J. Phys. Chem. B*, 2006, **110**, 13352.
37 H. S. Choi, W. Liu, P. Misra, E. Tanaka, J. P. Zimmer, B. I. Ipe, M. G. Bawendi and J. V. Frangioni, *Nat. Biotechnol.*, 2007, **25**, 1165.
38 W. Arap, R. Pasqualini and E. Ruoslahti, *Science*, 1998, **279**, 377.
39 Y. Lu, Y. Zhong, J. Wang, Y. Su, F. Peng, Y. Zhou, X. Jiang and Y. He, *Nanotechnology*, 2013, **24**, 135101.

 